Strain and damage analysis using high resolution digital image correlation in the stir zone of an AA6061-AA7075 dissimilar friction stir weld

Nicolas Dimov, Daniel Weisz-Patrault, Alexandre Tanguy, Thaneshan Sapanathan, Julien Benoist, Eric Charkaluk, Aude Simar

Strain and damage analysis using high resolution digital image correlation in the stir zone of an AA6061-AA7075 dissimilar friction stir weld

Nicolas Dimov [1,2,3], Daniel Weisz-Patrault [1], Alexandre Tanguy [1], Thaneshan Sapanathan [2, 4], Julien Benoist [3], Eric Charkaluk [1], Aude Simar [2]

[1] LMS, CNRS, Ecole Polytechnique, Institut Polytechnique de Paris, Palaiseau, France

[2] UCLouvain, iMMC, Louvain-la-Neuve, Belgium

[3] Thales Global Services (TGS), Vélizy-Villacoublay, France

[4] Curtin Corrosion Centre, WASM, Curtin University, Perth, Australia

Abstract

This work focuses on the strain and damage analysis of a micro tensile experiment of a AA6061-AA7075 dissimilar friction stir weld. Scanning electron microscopy combined with high resolution digital image correlation has been performed at two different scales to analyse strain fields and damage in the AA6061-AA7075 mixed region of the stir zone. Local alloy composition was identified as the critical parameter affecting the meso-scale strain distribution. At a finer scale, intermetallic particles also lead to strain localization within each individual alloy.

Keywords:

Dissimilar friction stir welding, Aluminium alloys, High Resolution Digital Image Correlation, Damage

1. Introduction

The friction stir welding (FSW) process enables the joining of metals in a solid state through friction and mechanical stirring [1]. A rotating tool is plunged at the interface between two clamped plates on either identical (similar welding) or different alloys (dissimilar welding) [2, 3]. The central stir zone experiences large plastic strains responsible for dynamic recrystallization [2, 4]. In dissimilar FSW of aluminium alloys, the stir zone exhibits strong heterogeneous alloy mixing resulting from the material flow associated to the tool complex

geometry. Both base materials are thus highly interconnected see e.g. Ref. [5] in 2024-7075 welds, or Ref. [6] (in particular their Figure 1) and Ref. [7] (in particular their Figure 6) in Al to Ti dissimilar welds. Dissimilar FSW has promising applications especially in the aerospace industry [2]. Extensive research has been conducted in the FSW literature to assess basic mechanical properties (hardness, yield strength, ultimate tensile strength, etc.) and sometimes studying fatigue properties [1,2,3].

Generally, digital image correlation (DIC) based techniques are employed to assess strain distribution under tension. Using a paint based marking technique and an optical camera setup, it is possible to generate strain maps at the macroscopic scale on the cross section of tensile samples of welded joints [8-29]. Suthar *et al.* [23] specifically studied strain localization in similar AA6061-AA6061 and dissimilar AA6061-AA7075 welds using optical camera DIC. In general, researches exploiting macroscopic scale DIC evidence the significant effect of strain localisation in the heat affected zone (HAZ), often the weak zone (e.g. in 6061 alloy [23]), on the tensile response. Hiscocks *et al.* [29] performed dissimilar magnesium FSW welds and were able to reach a slightly better resolution (> 240 µm) using improved optical cameras. This allowed them to evidence some heterogeneous deformations inside the nugget zone of their dissimilar welds but with large zones of uncaptured strain localisation. The research studies in Ref. [30–31] exploited a higher resolution DIC performed using optical cameras that can reach a resolution of typically 20 µm. However, no results are available at the scale of the bands of dissimilar materials that are typically observed in the stir zone of dissimilar friction stir welds nor at the scale of damage. This requires a DIC resolution below 1 µm or even below 100 nm and is the aim of the present paper.

To reach such a resolution, some micro or even nano-scale digital image correlation (DIC) experiments have been developed using scanning electron microscopy (SEM) rather than optical cameras [32–34]. Such high resolution analysis (called HR-DIC) is of great interest for studying localized strain distribution and damage mechanisms.

Our study investigates the local strain and damage distribution in a dissimilar aluminium 6061-7075 FSW joint and the effect of the mechanical properties and alloying elements of the base metals. To the best of the author’s knowledge, high resolution SEM based DIC has never been performed on dissimilar FSW joints.

2. Material and methods

A dissimilar weld 160 mm long composed of 6 mm thick AA6061-T651 and AA7075-T651 rolled plates are manufactured using a dedicated FSW machine. AA7075 is richer in Zn (5.29 wt%) than AA6061 (0.06 wt%). FSW parameters are optimized to avoid any major defects such as wormholes or kissing bonds, both being common in dissimilar FSW joints [35]. Pin length, rotational speed, advancing speed and vertical force are controlled to reach 5.75 mm, 400 rpm, 120 mm/min, and 10 kN respectively. Vickers hardness measurements were performed at mid-thickness of that weld on the transverse section with 1mm distance between indents and using a 200g load. As depicted in Figure 1(a,c), a single 55×6×1 mm^3 sample is extracted from the weld stir zone using a micro-cutting machine and has been polished up to 1 µm using a classical polishing routine. The analysed area has been selected to study strain partitioning between the two mixed alloys inside the stir zone. The sample is extracted from the cross-section orthogonal to the welding direction (Figure 1(c)). Different marking techniques are employed to perform the HR-DIC at two different scales, to capture strain at various scales, in between bands of aluminium alloys and at the scale of intermetallic particles:

1) In the central region of the weld, a gold pattern (Figure 1(d)) is deposited on a 600 µm×600 µm region using lithography. Diamond shaped markings spaced by 1 µm are used to form the pattern. A central 200 µm×200 µm square region is left empty.

2) The 200 µm×200 µm central region of the micro-grid is studied at a finer scale (Figure 1(d), zoom in blue square) using another pattern composed of randomly scattered 50 to 100 nm diameter tin speckles, and carried out via metal vacuum evaporation [36].

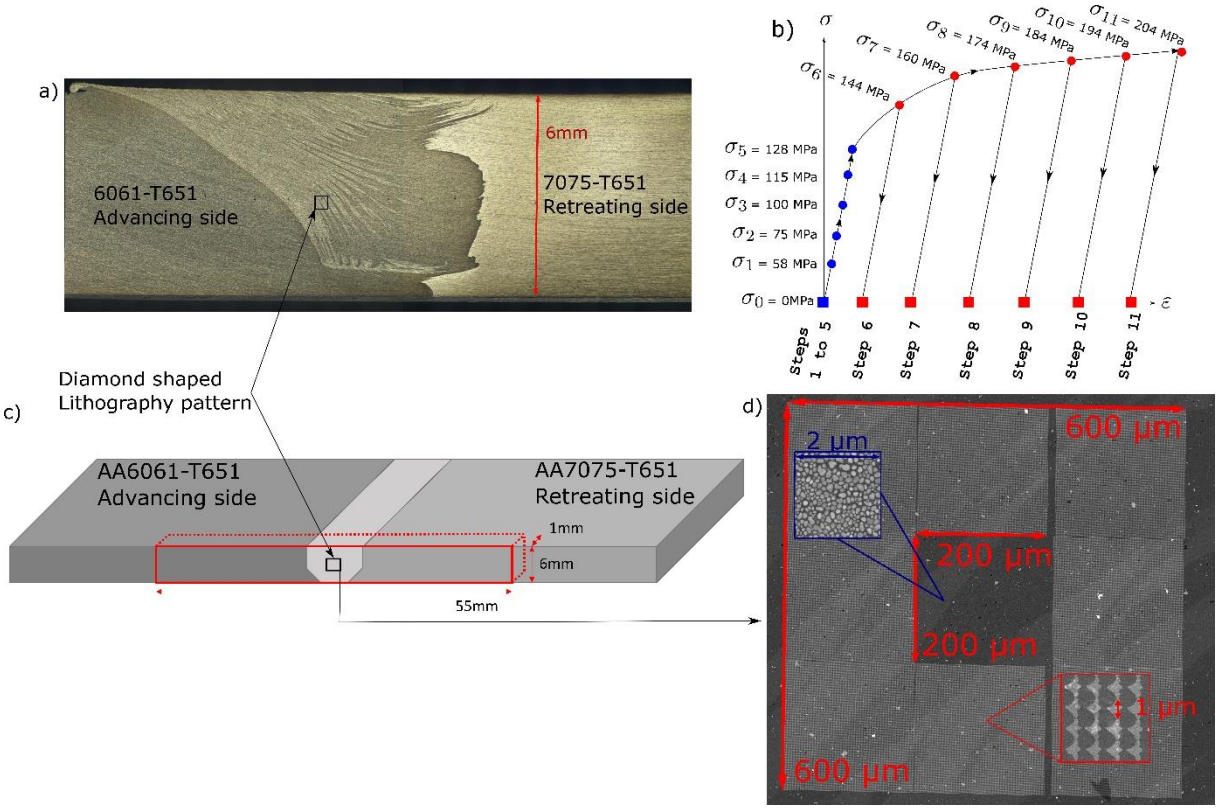

Figure 1: (a) Cross section of the weld and the selected DIC area. (b) Loading path with macroscopic stress/strain curve and imaging steps. (c) Sample extraction from the weld. (d) Gold micro-grid and tin random pattern (blue square).

The in situ tensile test is carried out by using a tensile machine inside a SEM. The measured macroscopic stress/strain curve is presented in Figure 1(b). SEM is used to acquire a total of 12 Back-Scattered Electron (BSE) images at different targeted steps of the deformation process. The BSE images are acquired in the cross section of the welded joint (Figure 1(c,d)) before applying the DIC markings. To minimize electronic noise generated by the tensile machine during the image acquisition process, the sample is elastically unloaded (Figure 1(b)). The gear mechanism used to apply the tensile load does not have a locking mechanism, thus the tensile machine cannot be shut down during sample loading. However, the electrical current in the tensile machine generates noise on the BSE images. Consequently, the samples must be unloaded to properly power off the tensile machine and acquire quality images. High resolution strain fields are computed by using a custom-made Correlation Manual Value (CMV) HR-DIC software [37]. The acquired BSE images are overlapped to the identified strain fields in order to associate strain and alloys distributions.

Figure 2(a,b) shows the Zn energy-dispersive X-ray spectroscopy (EDX) map in the stir zone. On EDX maps, the contrast gives an information on the local element composition. A brighter spot means more analysed element is present. Figure 2(b) shows how BSE contrast (Figure 2(a)) allows to qualitatively assess the local Zn content, and is sufficient to differentiate between AA6061 and AA7075 phases locally. Moreover Figure 2(c) shows a magnification of an area exhibiting both types of intermetallic particles present in AA6061 inside the stir zone: Mg-Si rich and Fe rich in black and white respectively in the BSE image.

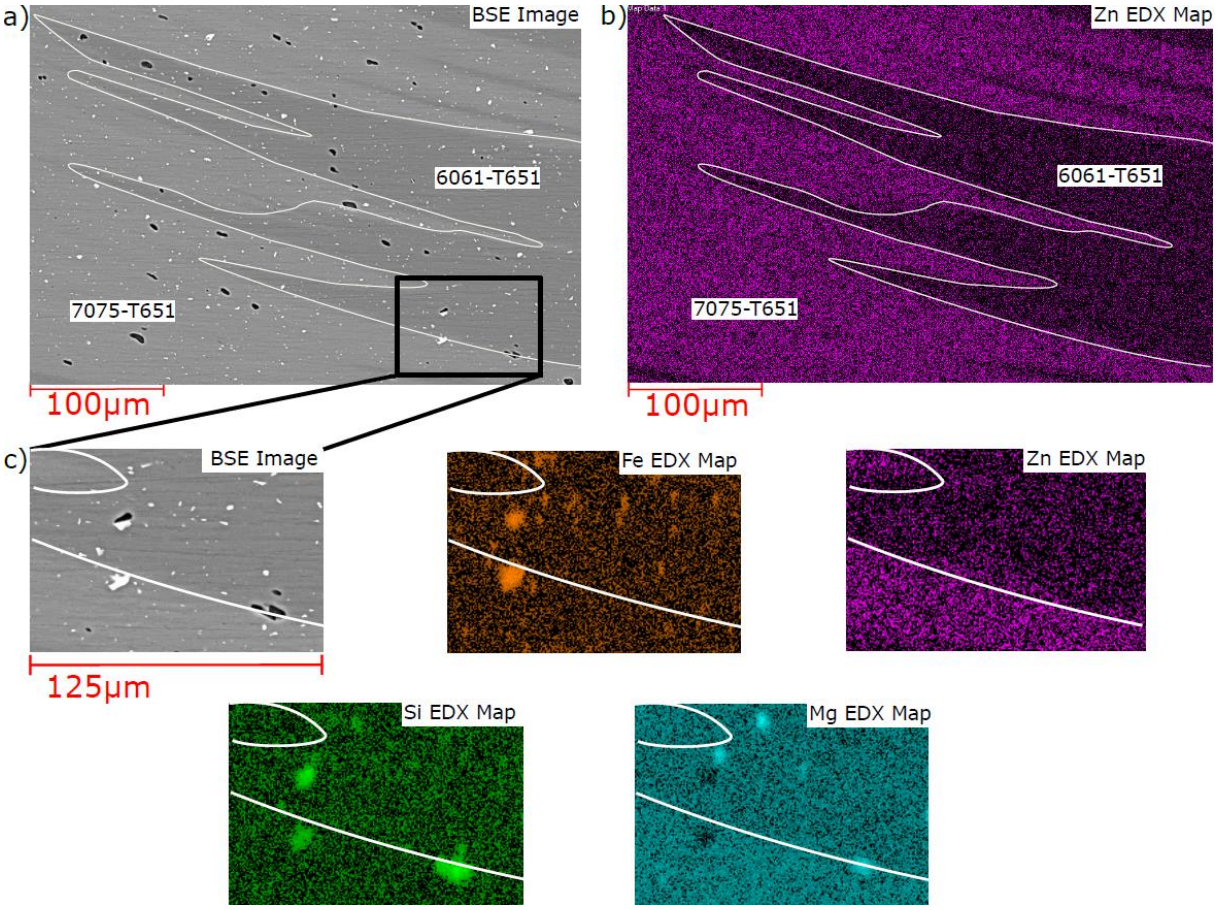

Figure 2: (a) BSE image taken in the centre of the stir zone between AA6061 and AA7075 and (b) EDX map showing the Zn distribution which enable to differentiate the AA7075 and AA6061 alloys. (c) A magnified zone from (a) showing two types of intermetallic particles: Fe rich (white) and Mg-Si rich (black) identified by the corresponding EDX maps.

3. Results and discussion

Figure 3 shows the hardness profile of the sample taken at the centreline of the cross section of the welded joint. A sharp difference in hardness values between the AA6061 (right) and

AA7075 (left) side of the welded joint is highlighted by a red circle. In the stir zone (evidenced by two vertical red lines), a local maximum is observed at a "distance from the centre of the weld" equal to 3 mm. This is the location where the HR-DIC sample was extracted. This hardness local maximum, coupled with the mixing of aluminium alloys on Figure 1(a), is the motivation to study local strain localization in that zone.

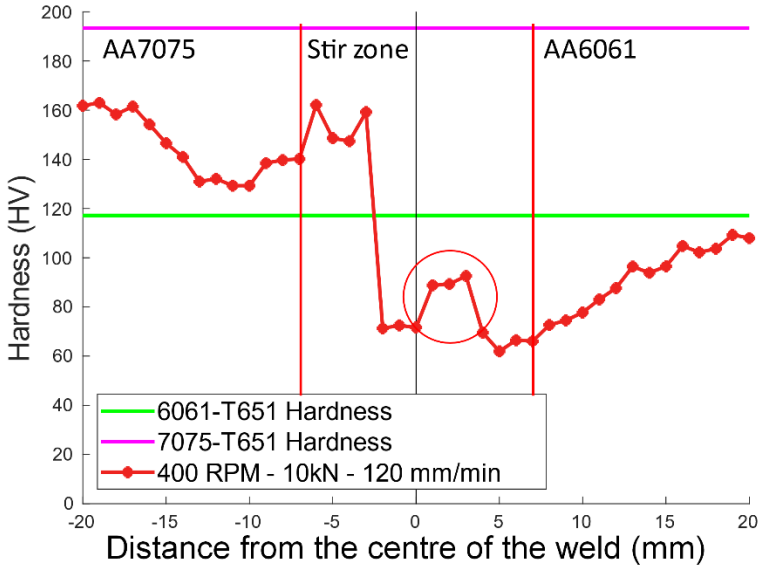

Figure 3: Hardness profile taken at the centre line of the studied AA6061-AA7075 FSW joint. The HR-DIC sample has been extracted in the red-circled zone.

BSE contrast in Figure 2(a) shows the AA6061 in a darker grey compared to the lighter AA7075, which reveals a mixing phase pattern composed of alternating layers of AA6061 and AA7075. This contrast allows the phase identification of Figure 4(a). A pattern with 1 µm spaced diamond shaped markings is well adapted to capture strain in both alloys while the finest speckle pattern in the central area is used to capture the local strain field at the micro Mg-Si and Fe rich particles scale.

Figure 4(a) shows the phase identification resulting from grey scale thresholding made with Image J software (AA6061 in red and AA7075 in blue). Using the diamond pattern, macroscopic strain fields in the stir zone are first measured (Figure 4(b)). Using Figure 4(a), an alloy composition can be attributed to each pixel of the image. A plastic strain value was also attributed to this pixel, using the DIC software. Figures 4(b) shows that the strain distribution is associated to the alloy's distribution pattern of Figure 4(a). A statistical analysis complements this observation, and box-plots representing plastic strain distribution for each

alloy at each loading step are provided in Figure 4(c). In the T651 state, yield strength (and ultimate tensile strength) are 240 MPa (290 MPa) and 460 MPa (540 MPa) for AA6061 and AA7075 respectively. As the yield strength of AA6061 is lower than the yield strength of AA7075, the AA6061 exhibits a higher mean value of plastic deformation for a given applied strain compared to the AA7075 when reaching the onset of plasticity (Figure 4(c)). This justifies the qualitative association between Figures 4(a) and 4(b). In addition, first and third quartiles enables to quantify in each alloy the statistical dispersion of plastic strain. As shown in Figure 4(c), this dispersion is qualitatively associated with the alloy's distribution pattern as it clearly increases with the applied stress for both alloys, but more significantly for the alloy with the lowest yield stress (i.e. AA6061). However, the significant strain heterogeneity taking place inside each alloy (and not only between both alloys) suggests that strain localization arises at a lower scale in each alloy. To support this impression more quantitatively, a simple variance decomposition of the plastic strain distribution is presented in Figure 4(d) to measure to what extend the alloy phases explain the strain dispersion. During elastic loading (i.e. steps 1 to 5), with similar elastic properties in both alloys, strain distribution is unaffected by the phase pattern (explained variance of 0%). Then, plastic strains gradually increase (i.e. steps 6 to 11), and tend to localize in the softest alloy. Consequently, the phase pattern explains an increasing part on the variation of strain accommodation, but partially as it only reaches 7% before fracture. Thus, most of the strain dispersion is due to strain localization among each phase, while only 7% of the strain dispersion occurred due to the fact that one alloy is softer than the other.

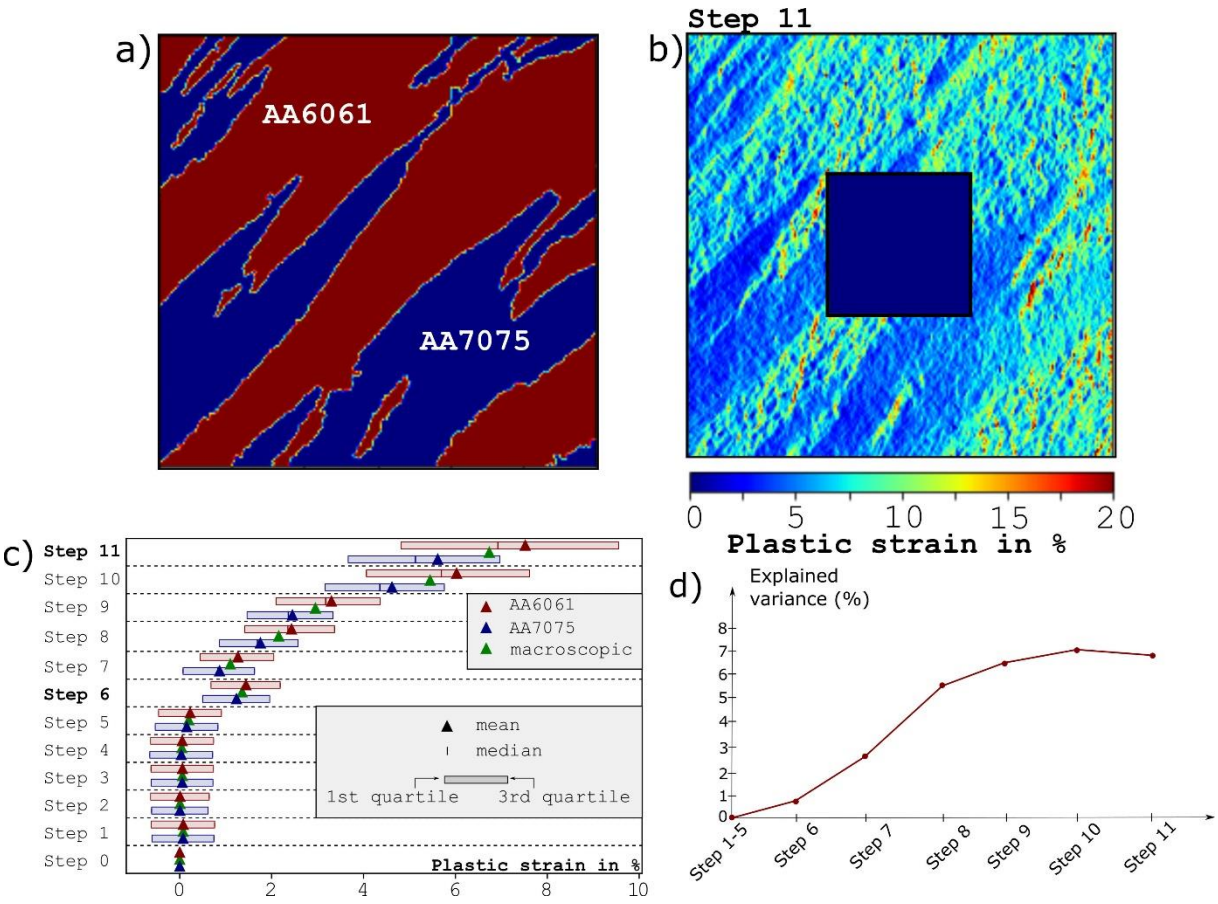

Figure 4: (a) Alloy distribution in the diamond shaped lithography area obtained by image segmentation. (b) Plastic strain field at step 11 in the diamond shape area. (c) Box-plots of plastic strain for each grade and for each loading step. (d) Percentage of the strain distribution variance explained by the phase pattern.

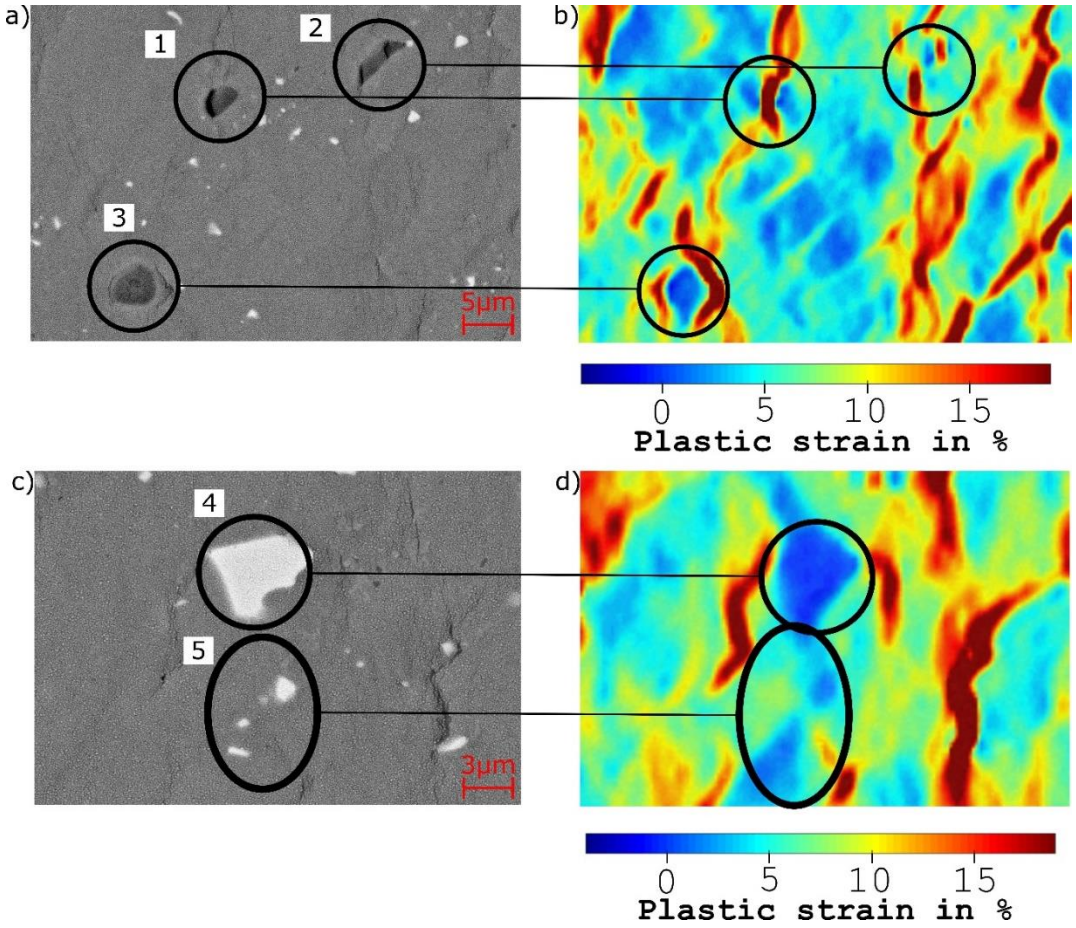

Figure 5: BSE imaging of Mg-Si (a) and Fe rich particles (c) along with their respective local strain maps (b,d). Multiple damage behaviours are identified and numbered: 1) Mg-Si rich inclusion decohesion from the Al matrix, 2) Mg-Si rich inclusion fracture, 3) Strong plastic strain localization, 4) Unbroken Fe inclusion, 5) Low plastic strain within a cluster of Fe rich particles.

Thus, local intragranular mechanisms likely explain the remaining part of the strain distribution variance. This is demonstrated here by the finer scale analysis within the AA6061 using the finer HR-DIC central grid (Figure 1(d)). Mg-Si and Fe rich particles are identified in the stir zone as shown in Figure 2(c) and 5(a,c). Local strain heterogeneities reported in Figures 5(b,d) are clearly associated to these intermetallic particles. On the basis of Figure 5, multiple deformation and damage mechanisms may explain the strain distribution: 1) decohesion between Mg-Si rich particles and the Al matrix, and 2) fracture of Mg-Si rich particles (highest strain values being located where decohesion and cracks appear), 3) strong plastic strain localization surrounding intermetallic particles, 4) unbroken hard Fe inclusion inducing a strong localization in the Al matrix, and 5) areas of relatively low plastic strain within clusters of Fe rich particles. Additionally, high plastic strain values are also observed in areas without

large intermetallic particles. Most likely, these plastic strain localization patterns are the result of the underlying microstructure, and particularly grain orientation and size [38]. However, no Electron Backscatter Diffraction (EBSD) data is available for this sample to make more than a hypothesis that grain size and orientation could explain this phenomenon.

4. Conclusions

A SEM in-situ tensile experiment conducted on a dissimilar AA6061-AA7075 assembly obtained by FSW is presented. High resolution digital image correlation has been performed at two different scales in the weld to characterise strain localization as a function of microstructural features. Mixing patterns of both Al alloys were quantitatively correlated with observed strain distribution and localization. However, this distribution explains only up to 7% of the variance just before failure. Thus, as the local AA6061 and AA7075 distribution is not sufficient to explain strain distribution, a finer scale damage analysis in the softest alloy revealed local damage and strain localization mechanisms, associated to Mg-Si and Fe rich particles.

Acknowledgments

The authors are grateful to the technical staff of the LACAMI technological platform of iMMC. Thales group and the ANRT are greatly acknowledged for funding the PhD of Nicolas Dimov.

References

[1] L. Murr, A review of FSW research on dissimilar aluminum alloys, J. Mater. Eng. Perform 19 (2010) 1071–1089. URL https://doi.org/10.1007/s11665-010-9598-0

[2] A. Heidarzadeh, S. Mironov, R. Kaibyshev, G. Çam, A. Simar, A. Gerlich, F. Khodabakhshi, A. Mostafaei, D. Field, J. Robson, A. Deschamps, P. Withers, Friction stir welding/processing of metals and alloys: A comprehensive review on microstructural evolution, Progress in Materials Science 117 (2021) 100752. URL https://doi.org/10.1016/j.pmatsci.2020.100752

[3] A. Simar, M.-N. Avettand-Fènoël, State of the art about dissimilar metal friction stir welding, Science and Technology of Welding and Joining 22 (2016) 389–403. URL https://doi.org/10.1080/13621718.2016.1251712

[4] Y. Sun, Y. Morisada, H. Fujii, N. Tsuji, Ultrafine grained structure and improved mechanical properties of low temperature friction stir spot welded 6061-T6 al alloys, Materials Characterization 135 (2018) 124–133. URL https://doi.org/10.1016/j.matchar.2017.11.0

[5] A. A. M. D. Silva, E. Arruti, G. Janeiro, E. Aldanondo, P. Alvarez, A. Echeverria, A. A. da Silva, E. Arruti, G. Janeiro, E. Aldanondo, P. Alvarez, A. Echeverria, Material flow and mechanical behaviour of dissimilar AA2024-T3 and AA7075-T6 aluminium alloys friction stir welds, Materials and Design 32 (4) (2011) 2021–2027. doi:10.1016/j.matdes.2010.11.059.

[6] A. Kar, S.V. Kailas, S. Suwas, Effect of Mechanical Mixing in Dissimilar Friction Stir Welding of Aluminum to Titanium with Zinc Interlayer, Transactions of Indian Institute of Metals, 72 (2019) 1533-1536 (2019). doi.org/10.1007/s12666-019-01643-x

[7] A. Kar, D. Yadav, S. Suwas, S.V. Kailas, Role of plastic deformation mechanisms during the microstructural evolution and intermetallics formation in dissimilar friction stir weld, Materials Characterization 164 (2020) 110371. doi.org/10.1016/j.matchar.2020.110371

[8] A. Simar, C. Jonckheere, K. Deplus, T. Pardoen, B. de Meester, Comparing similar and dissimilar friction stir welds of 2017–6005A aluminium alloys, Science and Technology of Welding and Joining 15 (3) (2010) 254–259. doi:10.1179/136217110x12665048207737.

[9] M.-N. Avettand-Fènoël, R. Taillard, G. Ji, Quality of interfaces in Cu/Al dissimilar friction-stirred welds, Vol. 706-709, 2012. doi:10.4028/www.scientific.net/MSF.706-709.959.

[10] H. JamshidiAval, S. Serajzadeh,N. Sakharova, A.Kokabi, A. Loureiro, A study on microstructures and residual stress distributions in dissimilar friction-stir welding of AA5086-AA6061, Journal of Materials Science 47 (14) (2012) 5428–5437. doi:10.1007/s10853-012-6430-2.

[11] E. Feistauer, L. Bergmann, L. Barreto, J. dos Santos, Mechanical behaviour of dissimilar friction stir welded tailor welded blanks in Al-Mg alloys for Marine applications, Materials and Design 59 (2014) 323–332. doi:10.1016/j.matdes.2014.02.042.

[12] M. I. Costa, D. Verdera, C. Leitão, D. M. Rodrigues, Dissimilar friction stir lap welding of AA 5754-H22/AA 6082-T6 aluminium alloys: Influence of material properties and tool geometry on weld strength, Materials and Design 87 (2015) 721–731. doi:10.1016/j.matdes.

2015.08.066.

[13] E. Feistauer, L. Bergmann, J. Dos Santos, Performance of friction stir welded Tailor welded blanks in AA5059 and AA6082 alloys for marine applications, Vol. 710, 2016. doi:10.4028/www.scientific.net/KEM.710.91.

[14] W. Noh, J. H. Song, I. J. Jang, S. H. Gwak, C. Kim, C. Y. Jung, Numerical and experimental investigation for formability of friction stir welded dissimilar aluminum alloys, IOP Conference Series: Materials Science and Engineering 418 (1) (2018). doi:10.1088/1757-899X/418/1/012056.

[15] T.Wang, M. Komarasamy, K. Liu, R. S. Mishra, Friction stir butt welding of strain-hardened aluminum alloy with high strength steel, Materials Science and Engineering A 737 (May) (2018) 85–89. doi:10.1016/j.msea.2018.09.035.

[16] G. Peng, Y. Ma, J. Hu, W. Jiang, Y. Huan, Z. Chen, T. Zhang, Nanoindentation Hardness Distribution and Strain Field and Fracture Evolution in Dissimilar Friction Stir-Welded AA 6061-AA 5A06 Aluminum Alloy Joints, Advances in Materials Science and Engineering 2018 (2018). doi:10.1155/2018/4873571.

[17] E. Feistauer, L. Bergmann, J. dos Santos, Effect of reverse material flow on the microstructure and performance of friction stir welded T-joints of an Al-Mg alloy, Materials Science and Engineering A 731 (2018) 454–464. doi:10.1016/j.msea.2018.06.056.

[18] G. Peng, Y. Ma, J. Hu, W. Jiang, Y. Huan, Z. Chen, T. Zhang, Nanoindentation Hardness Distribution and Strain Field and Fracture Evolution in Dissimilar Friction Stir-Welded AA 6061-AA 5A06 Aluminum Alloy Joints, Advances in Materials Science and Engineering 2018 (2018). doi:10.1155/2018/4873571.

[19] A. Barbini, J. Carstensen, J. F. dos Santos, Influence of a non-rotating shoulder on heat generation, microstructure and mechanical properties of dissimilar AA2024/AA7050 FSW joints, Journal of Materials Science and Technology 34 (1) (2018) 119–127. doi:10.1016/j.jmst.2017.10.017.

[20] T. Wang, H. Sidhar, R. S. Mishra, Y. Hovanski, P. Upadhyay, B. Carlson, Effect of hook characteristics on the fracture behaviour of dissimilar friction stir welded aluminium alloy and

mild steel sheets, Science and Technology of Welding and Joining 24 (2) (2019) 178–184. doi:10.1080/13621718.2018.1503801.

[21] N. A. Muhammad, C. S. Wu, Evaluation of capabilities of ultrasonic vibration on the surface, electrical and mechanical behaviours of aluminium to copper dissimilar friction stir welds, International Journal of Mechanical Sciences 183 (January) (2020) 105784. doi: 10.1016/j.ijmecsci.2020.105784.

[22] I. Scheider, A. Barbini, J. dos Santos, Numerical residual strength prediction of stationary shoulder friction stir welding structures, Engineering Fracture Mechanics 230 (2020). doi:10.1016/j.engfracmech.2020.107010.

[23] H. Suthar, A. Bhattacharya, S. K. Paul, Local deformation response and failure behavior of AA6061-AA6061 and AA6061-AA7075 friction stir welds, CIRP Journal of Manufacturing Science and Technology 30 (2020) 12–24. doi:10.1016/j.cirpj.2020.03.006.

[24] M. Geyer, V. Vidal, T. Pottier, C. Boher, F. Rézaï-Aria, Investigations on the material flow and the role of the resulting hooks on the mechanical behaviour of dissimilar friction stir welded Al2024-T3 to Ti-6Al-4V overlap joints, Journal of Materials Processing Technology 292 (2021). doi:10.1016/j.jmatprotec.2021.117057.

[25] H. Suthar, A. Bhattacharya, S. K. Paul, Determination of local constitutive properties in similar and dissimilar friction stir welded joints from DIC based surface strain measurement in two mutually perpendicular surfaces, Mechanics of Materials 160 (May) (2021) 103930. doi:10.1016/j.mechmat.2021.103930.

[26] I. Hadji, R. Badji, M. Gaceb, B. Cheniti, Dissimilar FSW of AA2024 and AA7075: effect of materials positioning and tool deviation value on microstructure, global and local mechanical behavior, International Journal of Advanced Manufacturing Technology 118 (7-8) (2022) 2391–2403. doi:10.1007/s00170-021-08120-0.

[27] Y. Uematsu, T. Kakiuchi, K. Niimi, P. Caiza, Local strain analysis under quasi-static tensile loading in Al/steel dissimilar friction stir weld by a digital image correlation method, International Journal of Advanced Manufacturing Technology 120 (1-2) (2022) 349–360. doi:10.1007/s00170-021-08481-6.

[28] H. Suthar, A. Bhattacharya, S. K. Paul, DIC-based approach to predict post necking behavior for AA6061, AA7075 and their friction stir welded joints, Mechanics of Materials 172 (2022) 104364. doi:10.1016/J.MECHMAT.2022.104364.

[29] J. Hiscocks, B. Diak, A. Gerlich, M. Daymond, Strain localisation and failure of dissimilar magnesium-based alloy friction stir welds, Science and Technology of Welding and Joining 23 (7) (2018) 628–634. doi:10.1080/13621718.2018.1450704.

[30] D. Texier, Y. Zedan, T. Amoros, E. Feulvarch, J. Stinville, P. Bocher, Near-surface mechanical heterogeneities in a dissimilar aluminum alloys friction stir welded joint, Materials and Design 108 (2016) 217–229. doi:10.1016/j.matdes.2016.06.091.

[31] M. Masoumi Khalilabad, Y. Zedan, D. Texier, M. Jahazi, P. Bocher, Effect of heat treatments on microstructural and mechanical characteristics of dissimilar friction stir welded 2198/2024 aluminum alloys, Journal of Adhesion Science and Technology 36 (3) (2022) 221–239. doi:10.1080/01694243.2021.1917868.

[32] F. Mas, G. Martin, P. Lhuissier, Y. Bréchet, C. Tassin, F. Roch, P. Todeschini, A. Simar, Heterogeneities in local plastic flow behavior in a dissimilar weld between low-alloy steel and stainless steel, Materials Science and Engineering: A 667 (2016) 156–170. doi:10.1016/J.MSEA.2016.04.082.

[33] Y. Balit, E. Charkaluk, A. Constantinescu, Digital image correlation for microstructural analysis of deformation pattern in additively manufactured 316L thin walls, Additive Manufacturing 31 (2020) 100862. doi:10.1016/J.ADDMA.2019.100862.

[34] C. C. Tasan, J. P. Hoefnagels, M. Diehl, D. Yan, F. Roters, D. Raabe, Strain localization and damage in dual phase steels investigated by coupled in-situ deformation experiments and crystal plasticity simulations, International Journal of Plasticity 63 (2014) 198–210. doi: 10.1016/J.IJPLAS.2014.06.004.

[35] N. Z. Khan, A. N. Siddiquee, Z. A. Khan, S. K. Shihab, Investigations on tunneling and kissing bond defects in FSW joints for dissimilar aluminum alloys, Journal of Alloys and Compounds 648 (2015) 360–367. doi:10.1016/J.JALLCOM.2015.06.246.

[36] M. Bourcier, M. Bornert, A. Dimanov, E. Héripré, J. L. Raphanel, Multiscale experimental investigation of crystal plasticity and grain boundary sliding in synthetic halite using digital

image correlation, Journal of Geophysical Research: Solid Earth 118 (2) (2013) 511–526. doi:10.1002/jgrb.50065.

[37] L. Allais, M. Bornert, T. Bretheau, D. Caldemaison, Experimental characterization of the local strain field in a heterogeneous elastoplastic material, Acta Metallurgica et Materialia 42 (11) (1994) 3865–3880. doi:10.1016/0956-7151(94)90452-9.

[38] W. Boas, M. Hargreaves, On the inhomogeneity of plastic deformation in the crystals of an aggregate. Proceedings of the Royal Society A 193 (1948) 89–97. https://doi.org/10.1098/rspa.1948.0035